Progress In Electromagnetics Research, Vol. 118, 185–203, 2011

ON THE FEASIBILITY OF THE LINEAR SAMPLING METHOD FOR 3D GPR SURVEYS

I. Catapano, F. Soldovieri, and L. Crocco*

National Research Council of Italy — Institute for Electromagnetic Sensing of the Environment, Via Diocleziano 328, Napoli 80124, Italy

Abstract—We discuss the applicability of the Linear Sampling Method (LSM) to GPR surveys carried out using array-based configurations. Since the images achieved via LSM are known to get worse when using a small number of antennas and a limited aperture, we introduce an analytic tool to foresee the expected LSM performance for a fixed array size and number of antennas. Notably, such a tool allows us to support (and appraise) the adoption of LSM to data collected with short arrays moved above the investigated domain, which is the configuration most viable in applications.

1. INTRODUCTION

The imaging of buried targets, underground structures and concealed objects is a challenging problem, which is relevant to geophysics, archaeology and civil engineering. In this framework, Ground Penetrating Radar (GPR) is a widely adopted tool [1], as it allows fast non-destructive and non-invasive surveys.

Traditional GPR images are obtained by joining radar echoes collected while moving the antennas along the measurement scan. However this simple procedure often does not provide detailed information on the subsurface and requires expert users interpretation. For this reason, several efforts have been addressed to develop GPR systems with improved performances, that is devices able to collect large amount of data by adopting multi-channel and/or array configurations [2–4] and imaging processing tools which not only allow to detect the targets, but also to reconstruct their morphology and, in very favorable conditions, their electromagnetic features [5–14].

An inverse scattering method of particular interest in this framework is the Linear Sampling Method (LSM) [15–17]. The

Received 27 April 2011, Accepted 20 June 2011, Scheduled 1 July 2011

* Corresponding author: Lorenzo Crocco (crocco.l@irea.cnr.it).

LSM can image the morphological features of single or multiple objects (dielectric and/or metallic) from single frequency scattered field data, without requiring approximations and a priori information. In addition, the LSM is based on the solution of a linear inverse problem [18], so that it is free from so-called "false" solutions, which affect non-linear approaches and is very effective in terms of computational requirements. On the other hand, the LSM requires that scattered field data are collected under a *multi-view multi-static* (MV-MS) arrangement, in which multiple positions of the transmitting antennas are exploited and, for each of them, the backscattered field is recorded at several locations.

The aforementioned recent development of array based systems allows MV-MS data collection also in GPR, thus making the adoption of LSM feasible in such a framework. On the other hand, the reconstruction capabilities of LSM are extremely good when a large number of antennas is considered, while they deteriorate as long as the number of antennas or the aperture of the array are reduced [8, 15, 17, 19]. Hence, it is important to devise the constraints to follow in the design of the measurement setup, and in particular to understand the conditions under which LSM can achieve satisfactory results, while keeping the system's complexity low.

To this end, we introduce an "expected performance index" based on the spectral analysis of the integral operators relevant to the scattering phenomenon at hand, which allows us to foresee the reconstruction capabilities of the LSM as a function of the array aperture. In particular, the proposed tool provides information on the spatial region that can be actually imaged via LSM by means of an array having fixed size and number of elements. Notably, the proposed index also supports the feasibility of a strategy to apply the LSM when the GPR data are collected by moving the array above the investigated region, thus allowing a further reduction of the complexity of the measurement set-up.

The paper is organized as follows. In the next Section, the LSM is briefly reviewed. The performance expectation tool is introduced in Section 3 and the strategy to apply LSM to data collected with a moving array is described in Section 4. In Section 5, some numerical examples are provided, followed by concluding remarks.

2. THE LINEAR SAMPLING METHOD

2.1. Mathematical Formulation

The reference scenario considered for the formulation of the electromagnetic scattering problem at hand is shown in Fig. 1.

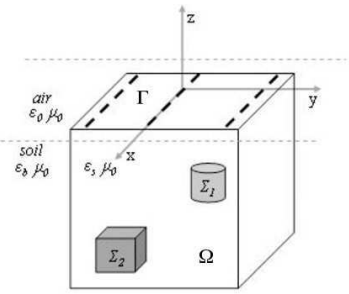

Figure 1. Geometry of the problem: the dashes represent the antennas of the GPR array.

The investigated region Ω is embedded into a lossy soil with complex permittivity ε_b and hosts targets having arbitrary complex permittivities ε_s, whose support is denoted as Σ. All the considered materials are non magnetic.

Since linearly polarized antennas are commonly used in GPR surveys, the LSM formulation is here reviewed with respect to this configuration, while we address the reader to [20] for a multi-polarization formulation of the LSM for a half-space geometry.

Let p be the considered polarization, the single frequency scattered field data are gathered under a MV-MS configuration by means of a 2-D antennas array in which the antennas positions correspond to a 2-D grid of points that partitions the measurement surface Γ. Assuming N transmitting and receiving antennas, the whole measurement process provides the $N \times N$ multistatic response data matrix (MRM), $\mathbf{E}_s$, whose generic element E^s_{mn} is the p component of the scattered field at the m-th receiver when the n-th source is transmitting.

To image the buried targets by using the LSM, one has first to sample the investigated domain Ω into an arbitrary (finite) set of *sampling* points, $\underline{r}_s \in \Omega$. Then, in each of them, one has to solve the linear ill-conditioned system:

$$\mathbf{E}_s\left[\mathbf{x}(\underline{r}_s)\right] = \mathbf{g}_{BG}(\underline{r}_s), \tag{1}$$

where $\mathbf{x}$ is the N dimensional unknown vector and $\mathbf{g}_{BG}$ is the N-dimensional vector that contains the values of the p-component of the Green's function for the assumed reference scenario [21], that is the field radiated at the N receivers on Γ by an elementary source located at $\underline{r}_s$ in Ω (when the targets are not present).

The regularized solution of (1) on the sampling grid provides an estimate of the unknown targets' shapes since, in each sampling point, the L^2-norm of the vector, $\|\mathbf{x}(\underline{r}_s)\|$, exhibits a different behavior if the

point is inside or outside of the targets [15]. In particular, $\|\mathbf{x}(\underline{r}_s)\|$ assumes its largest values when $\underline{r}_s \notin \Sigma$, whereas it assumes low values in points which are internal to the targets. As such it plays the role of a *support indicator*.

The expression of this indicator, in the following refereed as *LSM indicator*, can be obtained by solving Eq. (1) via Singular Value Decomposition (SVD) [18], that is:

$$X(\underline{r}_s) = \|\mathbf{x}(\underline{r}_s)\|^2 = \frac{1}{\|\mathbf{g}_{BG}(\underline{r}_s)\|^2} \sum_{n=1}^{N} \left(\frac{\sigma_n}{\sigma_n^2 + \alpha} \right)^2 \|\langle \mathbf{g_{BG}}(\underline{r}_s), \mathbf{u_n} \rangle\|^2, \quad (2)$$

where σ_n denote the singular values of the matrix $\mathbf{E}_s$ ordered for decreasing magnitudes and accumulating to zero as $N \to \infty$, $\mathbf{u_n}$ are the corresponding left singular vectors and $< \cdot, \cdot >$ denotes the scalar product for the complex vectors. The Tikhonov regularization parameter α is computed according to the empirical criterion proposed in [22], which does not require an explicit knowledge of the noise level. The normalization factor in front of the summation is introduced to compensate for the effect of limitation in aspect [20].

It is worth to remark that the main computational effort required by LSM is the evaluation of the SVD of $\mathbf{E}_s$. However, since the matrix dimension is dictated by the number of antennas, such an effort would be almost negligible even for a full 3-D reconstruction.

Finally, note that the orientation of the elementary source radiating the field at the right-hand side of (1) is arbitrary. Accordingly, Eq. (1) is representative of three equations, one for each orientation of the source [20]. However, in the following we only consider a right-hand side parallel to the incident field polarization. Based on our experience, this is the main contribution to the indicator [20].

3. LSM PERFORMANCE FOR A LIMITED APERTURE

As mentioned in the Introduction, the performance of LSM becomes quite poor when simplified measurement configurations are used. The analogy between LSM and focusing problems [17] allows to explain this circumstance. As a matter of fact, if the number of antennas constituting the array is low or if they are not properly spaced, it will be not possible to correctly focus the incident field. Moreover, using few receivers corresponds to match the two sides of Eq. (1) only in a few points. As a consequence, the indicator may not provide reliable images of the investigated scenario.

As far as the antennas spacing is concerned, the peculiar nature of the GPR configuration at hand, in which the antennas work at a

single frequency and are located very close to the air-soil interface, suggests that a practical (sub-optimal) sampling rule is to fix the antennas' spacing Δ according to the Nyquist-Shannon criteria. In particular, one can sample the field considering that propagation occurs in a homogeneous medium having the electric properties of the soil. Accordingly, $\Delta = \lambda_b/2$, λ_b being the wavelength in the probed soil at the considered frequency.

Assuming such a criterion, the number of antennas uniquely identifies the array aperture, and the question arises of understanding which is the spatial region that can be properly imaged via LSM with such an array. To this end, we will consider two figures of merit which can be used to characterize the scattering phenomenon underlying the GPR survey and the LSM processing:

- the first one is the *probing wave footprint*, which identifies the region wherein the array is able to radiate a significant (in energy) incident field, that is obviously a necessary condition to induce a backscattering from the buried targets;
- the second one is the "sampling point footprint", that represents the capability of an elementary source located in the sampling point to radiate a significant field (in energy) at the receivers. As detailed in Section 3.2 the observation of this quantity allows us to determine the region which can be imaged via LSM.

In the following, we introduce these quantities by relying on the spectral properties of the two semi-discrete integral operators that describe the scattering phenomenon in the configuration at hand.

3.1. The Probing Wave Footprint $\mathcal{T}$

The first operator we consider relates the currents feeding the N antennas located on Γ to the incident fields they radiate in Ω. Such an operator is defined as:

$$\mathcal{A}_i^{pp} : \mathbf{i}_{TX}^p \rightarrow E_{inc}^p(\underline{r}) = \sum_{m=1}^{N} \mathbf{G}^{pp}(\underline{r}_m, \underline{r}) \mathbf{i}_{TX}^p(\underline{r}_m) \tag{3}$$

where E_{inc}^p denotes the p-component of the incident field radiated in Ω by N p-oriented sources located in $\underline{r}_m \in \Gamma$, $m = 1, \ldots, N$, fed by the N dimensional current vector $\mathbf{i}_{TX}^p$.

Let $\{\mathbf{s}_n, \zeta_n, f_n\}$ be the SVD of $\mathcal{A}_i^{pp}$, the generic p polarized incident field in Ω can be expressed as a linear combination of the singular functions $\{f_n\}$:

$$E_{inc}^p(\underline{r}) = \mathcal{A}_i^{pp} \left[\mathbf{i}_{TX}^p\right] = \sum_{n=1}^{N} \zeta_n^N \left\langle \mathbf{i}_{TX}^p, \mathbf{s}_n \right\rangle f_n(\underline{r}). \tag{4}$$

Accordingly, its square amplitude in each $\underline{r} \in \Omega$ is:

$$|E^p_{inc}(\underline{r})|^2 = \left|\sum_{n=1}^{N} \langle E^p_{inc}, f_n\rangle f_n(\underline{r})\right|^2 = \left|\sum_{n=1}^{N} a_n^N f_n(\underline{r})\right|^2 \leq \sum_{n=1}^{N} \left|a_n^N\right|^2 \sum_{n=1}^{N} |f_n(\underline{r})|^2 . \tag{5}$$

Hence, the singular functions $\{f_n\}$ can be used to determine the portion of Ω that can be investigated by means of N transmitting antennas. As a matter of fact, their "spatial content" [23]:

$$\mathcal{T}(N, \underline{r}) = \sum_{n=1}^{N} |f_n(\underline{r})|^2 \tag{6}$$

provides information on the energy radiated in any $\underline{r} \in \Omega$ by the N transmitters and therefore represents the *array footprint*. In particular, objects located in those parts of Ω wherein $\mathcal{T}(N, \underline{r})$ is negligible are expected to be weakly involved in the scattering phenomenon and thus their contribution to the MRM data matrix will be almost negligible and/or overwhelmed by noise.

3.2. The Sampling Point Footprint $\mathcal{R}$

Let us define as:

$$\mathcal{A}_e^{pp} : J^p(\underline{r}) \rightarrow \mathbf{e}^p_{RX}(\underline{r}_m) = \int_\Omega \mathbf{G}^{pp}(\underline{r}, \underline{r}_m) J^p(\underline{r}) d(\underline{r}) \tag{7}$$

the integral operator that relates the volumetric currents induced in the investigated region to the field they radiate at the receivers. This operator gives the values of the p-component of the scattered field at N points $\underline{r}_m$ on Γ, due to a p-oriented current induced in Ω.

Since we are assuming that the transmitting and receiving antennas are located at the same positions, Lorentz reciprocity entails that the SVD of $\mathcal{A}_e^{pp}$ is the same as that of $\mathcal{A}_i^{pp}$, but for an exchange in the role of the left and right singular functions. Accordingly, the field radiated in the generic point $\underline{r}_m$ on Γ can be expressed as:

$$\mathbf{e}^p_{RX}(\underline{r}_m) = \mathcal{A}_e^{pp}\left[J^p(\underline{r})\right] = \sum_{n=1}^{N} \zeta_n^N \langle J^p, f_n\rangle \mathbf{s}_n(\underline{r}_m). \tag{8}$$

By taking advantage of this decomposition, it is possible to express the volumetric current corresponding to a p-oriented elementary dipole

located in $\underline{r}_s$, $J_\delta(\underline{r}) = \delta(\underline{r} - \underline{r}_s)$, as:

$$J_\delta(\underline{r}) = \sum_{n=1}^{N} \langle J_\delta, f_n \rangle f_n(\underline{r}) = \sum_{n=1}^{N} [f_n(\underline{r}_s)]^* f_n(\underline{r}), \tag{9}$$

where * stands for the conjugation.

Then, we can compute the energy of the field radiated by $J_\delta(\underline{r})$, applied in $\underline{r}_s$, at the N measurement points on Γ, that is, the footprint of the sampling point. In particular, taking into account the orthonormality of the singular vectors $\{\mathbf{s}_n\}$:

$$\mathcal{R}(N, \underline{r}_s) = \left\| \mathbf{e}^p_{RX} \right\|^2 = \langle \mathcal{A}^{pp}[J_\delta], \mathcal{A}^{pp}[J_\delta] \rangle = \sum_{n=1}^{N} [\zeta_n]^2 \left| f_n(\underline{r}_s) \right|^2 \tag{10}$$

The observation of this function $\forall \underline{r} \in \Omega$ allows to appraise which parts of the investigated domain can be imaged via LSM. As a matter of fact, when the sampling point is located in the sub-domain D of Ω where $\mathcal{R}(N, \underline{r})$ is negligible, the field radiated on Γ by $J_\delta(\underline{r})$ will vanish. Since this field is the right hand side of Eq. (1), the linear system to solve in each $\underline{r}_s \in D$ becomes homogeneous, so that any linear combination of the measured data with vanishing coefficients will be able to provide a solution of the LSM equation. As a consequence, the LSM indicator $X(\underline{r}_s \in D)$ will not be anymore able to discriminate between points belonging to the targets and points lying outside of them, being vanishing everywhere in D without any relation to the target support.

3.3. The LSM Expected Performance Index $\mathcal{E}$

The quantities introduced in the previous sub-sections take into account two different aspects which come into play in the processing underlying the application of LSM to GPR surveys. Hence, when considering a sampling point in the region under test, the LSM will be capable of imaging that point if *both* the footprints are therein meaningful. As such, we introduce the *expected performance index* defined as:

$$\mathcal{E}(N, \underline{r}) = 10 \log_{10} \left[\frac{\mathcal{T}(N, \underline{r}) \mathcal{R}(N, \underline{r})}{\max_{\underline{r} \in \Omega} [\mathcal{T}(N', \underline{r}) \mathcal{R}(N', \underline{r})]} \right]^{\frac{1}{2}}, \tag{11}$$

which allows to foresee which sub-domain of Ω can be properly imaged by means of an array of N elements evenly spaced by $\lambda_b/2$. In (11), N' denotes the number of antennas of an array having the same size as the transverse dimension of Ω, which we assume as the maximum array aperture.

4. DATA COLLECTED WITH A MOVING ARRAY

With the aim of reducing as much as possible the complexity of the measurement set-up, in this Section we introduce a strategy to apply the LSM when data are collected by means of an array of fixed length smaller than the transverse extent of the investigated region, which is moved above this region. Such an arrangement is of interest when 3-D GPR surveys are performed, as often in practice, by means of a linear array (rather than using a 2-D one) or when, in the 2-D geometry, a short array is used to collect data along a profile.

A possible way to apply LSM in this case would be to evaluate the support indicator in the region below the physical array and then juxtapose the maps. However, such an approach requires the interpolation of the obtained slices (in the 3-D case) and the definition of a rule to combine maps corresponding to different indicators.

To avoid both issues, we propose a strategy in which Eq. (1) is still considered and the elements of the MRM corresponding to transmitter receiver pairs for which the scattered field is not measured are simply replaced with zeroes. By doing so, we can achieve a single indicator map, at the cost of a slight increase of the computational cost. As it will be shown through numerical examples, this strategy allows to achieve satisfactory performances when applying the LSM to extremely simplified configurations.

To appraise the imaging capabilities of LSM in this configuration, we can again take advantage of the previously introduced tools. By denoting with P the number of positions in which the N elements array is moved, we can build the probing wave footprint $\mathcal{T}_j(N, \underline{r})$ for each array position $j = 1, \ldots, P$ and obtain the overall area spanned by the probing waves through the combined map:

$$\tilde{\mathcal{T}}(N, P, \underline{r}) = \frac{1}{P} \sum_{j=1}^{P} \mathcal{T}_j(N, \underline{r}). \tag{12}$$

Conversely, a single footprint with respect to all the receivers' positions has to be considered for each sampling point, $\mathcal{R}(N \times P, \underline{r})$.

The resulting expected performance index is then:

$$\tilde{\mathcal{E}}(N, P, \underline{r}) = 10 \log_{10} \left[\frac{\tilde{\mathcal{T}}(N, P, \underline{r}) \mathcal{R}(N \times P, \underline{r})}{\max_{\underline{r} \in \Omega} [\mathcal{T}(N', \underline{r}) \mathcal{R}(N', \underline{r})]} \right]^{\frac{1}{2}}. \tag{13}$$

5. NUMERICAL EXAMPLES

In the following, we show some numerical examples concerning the imaging of buried voids. In particular, an example in the 2-D case

is given to describe the use of the above tools, while an example concerning a full 3-D survey is given to assess the reconstruction capabilities of the LSM in a problem relevant to GPR surveys.

5.1. 2-D Scalar Case

The region under test Ω is a rectangular domain embedded in a lossy soil, whose complex permittivity has average value $\varepsilon_b = 4 - i0.06$. This investigated domain is $10\lambda_b \times 5\lambda_b$ large, λ_b being the wavelength at 300 MHz with respect to the real part of the soil's average permittivity. Such a domain is discretized in a grid of 100×50 sampling points. The transmitting and receiving antennas are located at the air-soil interface on a rectilinear domain Γ and are spaced of $\lambda_b/2$.

First of all, let us observe the maps of $\mathcal{E}(N, \underline{r})$, defined in (11), obtained in this scenario for different values of N, Figs. 2(a)–(d), related to arrays centered with respect to the investigation domain.

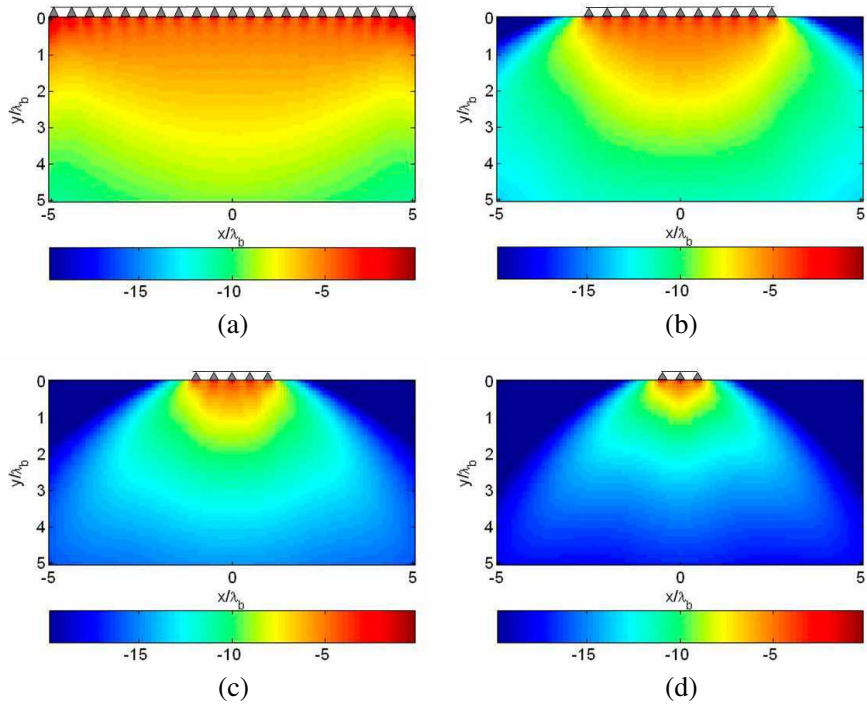

Figure 2. 2-D expected LSM performance index for different values of N: (a) $\mathcal{E}(21, \underline{r})$; (b) $\mathcal{E}(11, \underline{r})$; (c) $\mathcal{E}(5, \underline{r})$; (d) $\mathcal{E}(3, \underline{r})$.

Leaving aside feasibility considerations, from these plots one can notice that an array having $N = 21$ antennas is expected to be suitable to image the whole region under test Ω, whereas using $N = 3$ antennas it is only possible to reliably image a very reduced portion of Ω (just underneath the array). Moreover, due to the quickly decreasing behavior of $\mathcal{E}(N, \underline{r})$ in depth, when reducing N, one expects to miss the detection of objects located far from the measurement line Γ.

To verify these indications, we have considered the imaging of six air-gaps having different size and location, see Fig. 3(a). Synthetic scattered field data have been generated by using a method of moment forward solver and corrupted by additive Gaussian noise, with signal-to-noise ratio $SNR = 25\,\mathrm{dB}$.

Figure 3(b) shows the map of the normalized logarithmic LSM indicator, defined as in (2), for $N = 21$ and confirms that a $10\lambda_b$ long measurement line allows to detect and locate all the objects in

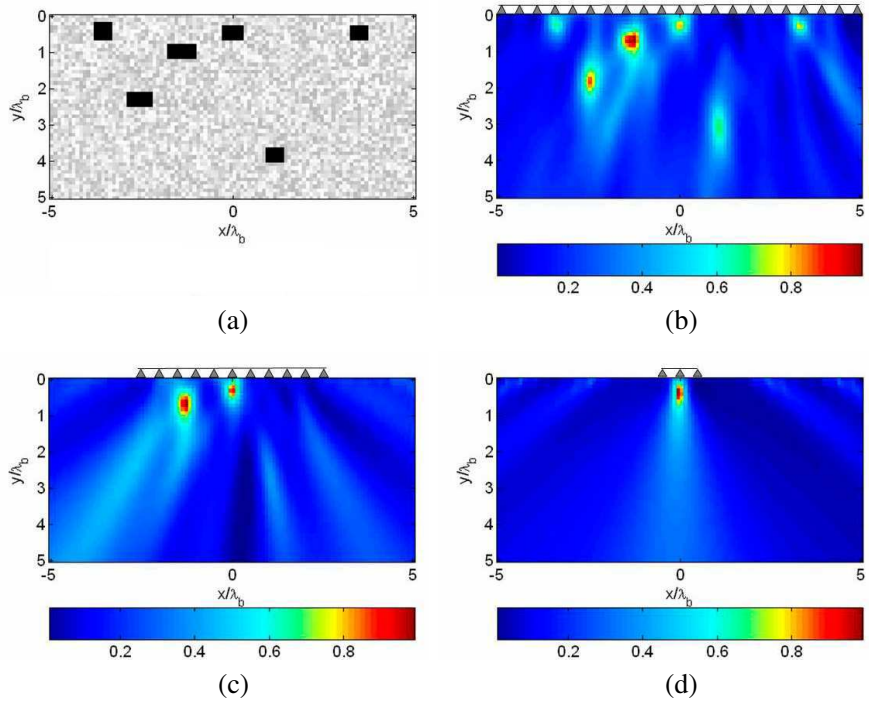

Figure 3. (a) Reference scenario; LSM indicator map for various values of N: (b) $N = 21$; (c) $N = 11$; (d) $N = 3$. The plotted function is $[X/X_{\max}]^{-1}_{dB}$.

Ω. In particular, one can appraise the different size and position of the various targets even if a slight error occurs on the localization of deeper ones. It is also interesting to observe the LSM indicators for $N = 11$ and $N = 3$, Figs. 3(c), (d), respectively. In these cases, not all targets are detected and the properly imaged ones indeed lie in those regions where $\mathcal{E}(11, \underline{r}_s)$ and $\mathcal{E}(3, \underline{r}_s)$ are larger than -10 dB (see Figs. 2(c), (d)). It is worth to note that similar results are observed considering a larger amount of noise (but for an obvious degradation of the images).

The same imaging problem has been also tackled with data collected by means of 3 antennas array swiped along the air-soil interface. The $10\lambda_b$ profile is covered by shifting the 3-elements array

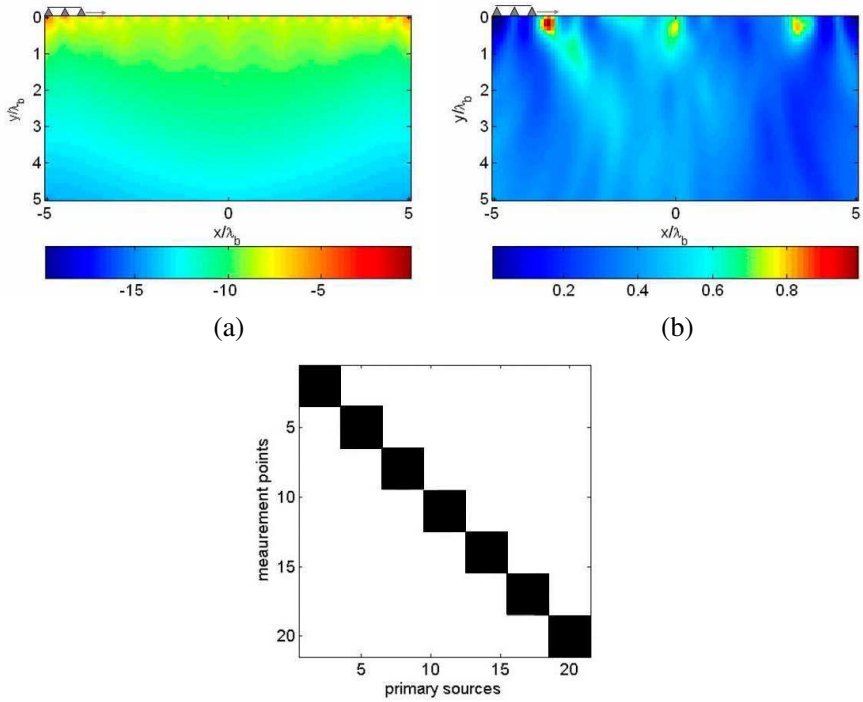

Figure 4. LSM via a moving array: (a) Expected performance index $\tilde{\mathcal{E}}(3, 7, \underline{r})$; (b) map of $[X/X_{\max}]_{dB}^{-1}$; (c) processed MRM data matrix, the black pixels represent the measured data. The other elements of the matrix are equal to zero.

in 7 different positions. The expected performance index $\tilde{\mathcal{E}}(3, 7, \underline{r}_s)$, Eq. (13), pertaining to this configuration is shown in Fig. 4(a). From this plot, one can foresee that the proposed simple strategy allows to enlarge the area that can be imaged, even if, due to the reduced aperture of the moving array, the deeper part of Ω is still not properly probed. This expectation is confirmed by the obtained LSM indicator map, Fig. 4(b). As a matter of fact, only the targets located in the shallower portion of Ω are successfully imaged, while the other ones, being located in the subregion $D \subset \Omega$ where $\tilde{\mathcal{E}}(3, 7, \underline{r}_s)$ is negligible, are either missed or not accurately localized. To further appraise the obtained result, the processed MRM data matrix is displayed in Fig. 4(c), to show that indeed only a few elements of the complete matrix ($N = 21$) are actually exploited with the proposed strategy.

5.2. 3-D Vectorial Case

Let us now consider the application of the LSM to a 3-D GPR survey. At the frequency of 200 MHz, we consider a cubic region embedded in a soil of complex permittivity $\varepsilon_b = 5 - i0.09$. The investigated region has side $2.2\lambda_b$ and it is probed by means of $N \times N$ y-oriented electric dipoles. The y-component of the scattered field is collected in the same $N \times N$ positions. The domain Ω is discretized into a grid of $22 \times 22 \times 22$ sampling points and, in each of them Eq. (1) is solved, taking as right hand side the y-component of the field radiated by an y-oriented electric dipole located in sampling point. Under these hypotheses, the SVD of $\mathcal{A}_i^{yy}$ ($\mathcal{A}_e^{yy}$) is exploited to determine the portion of Ω which can be actually imaged in this configuration.

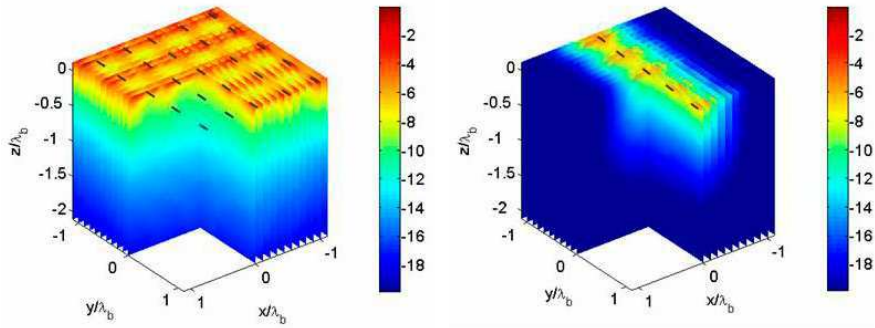

(a) (b)

Figure 5. Expected performance index $\mathcal{E}(N, \underline{r})$: (a) $N = 25$ antennas; (b) $N = 5$ antennas.

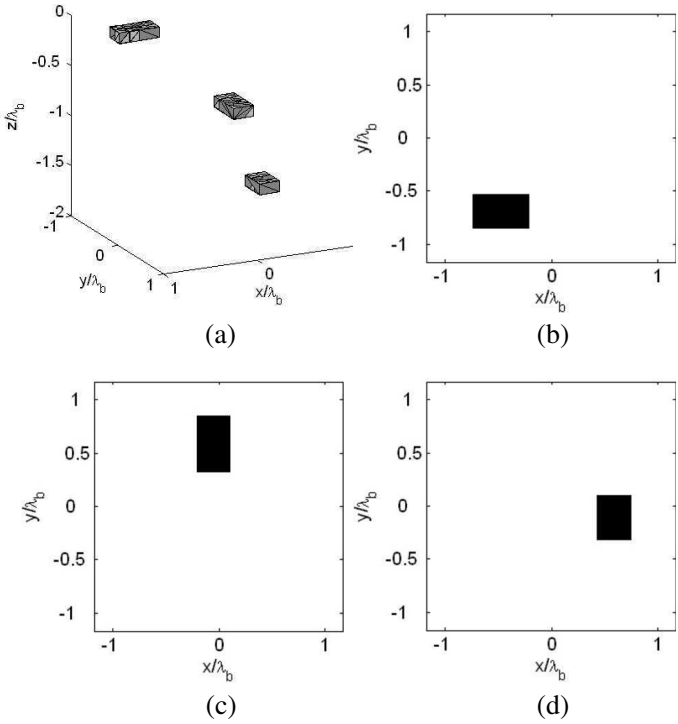

Figure 6. Reference scenario: (a) 3-D view; (b) slice at $z = -0.3\lambda_b$; (c) slice at $z = -0.7\lambda_b$; (d) slice at $z = -1.6\lambda_b$.

The plot of $\mathcal{E}(N, \underline{r})$ corresponding to a 2-D array using $N = 25$ antennas evenly spaced by $\lambda_b/2$ is shown in Fig. 5(a), while the one of a linear array of $N = 5$ antennas at $x = 0$ is shown in Fig. 5(b).

These figures suggests that only a very reduced portion of the domain under test can be imaged by using a linear array of $N = 5$ elements. In particular, deeper objects are expected to be missed and, due to the lack of illumination and measurement diversity, a loss of accuracy in the direction orthogonal to the measurement line is expected.

To verify these indications we have considered the scenario sketched in Fig. 6, in which three empty cavities are embedded in the background medium. The cavities have size $0.5\lambda_b \times 0.3\lambda_b \times 0.2\lambda_b$, $0.3\lambda_b \times 0.5\lambda_b \times 0.2\lambda_b$ and $0.4\lambda_b \times 0.4\lambda_b \times 0.2\lambda_b$, respectively, and their centers are at $0.3\lambda_b$, $0.7\lambda_b$ and $1.6\lambda_b$ below the interface (Figs. 6(b)–(d) show the central slice of the targets). As in the 2-D case, synthetic data have been generated by means of a method of moment forward solver

and corrupted by means of an additive Gaussian noise, $SNR = 25\,\mathrm{dB}$.

Figure 7(a) shows the 3-D map of the normalized logarithmic support indicator X achieved by processing data collecting by using the full grid ($N = 25$), while its slices corresponding to the center of the targets are given in Figs. 7(b)–(d). In these figures, as in the following ones, the dashed lines represent the actual contours. In agreement with the performance expected from Fig. 7(a), the LSM is able to detect all the objects and provides an accurate morphological reconstruction of the shallower ones, while the shape of the deeper target is roughly retrieved.

On the other hand, as suggested by Fig. 5(b), the performances worsen when a linear array of $N = 5$ antennas is used, see Figs. 8(a)–(d). As a matter of fact, the deep target is completely missed and the size of the shallower objects in the (x-y) plane is overestimated.

When considering data gathered when moving the 5 antennas

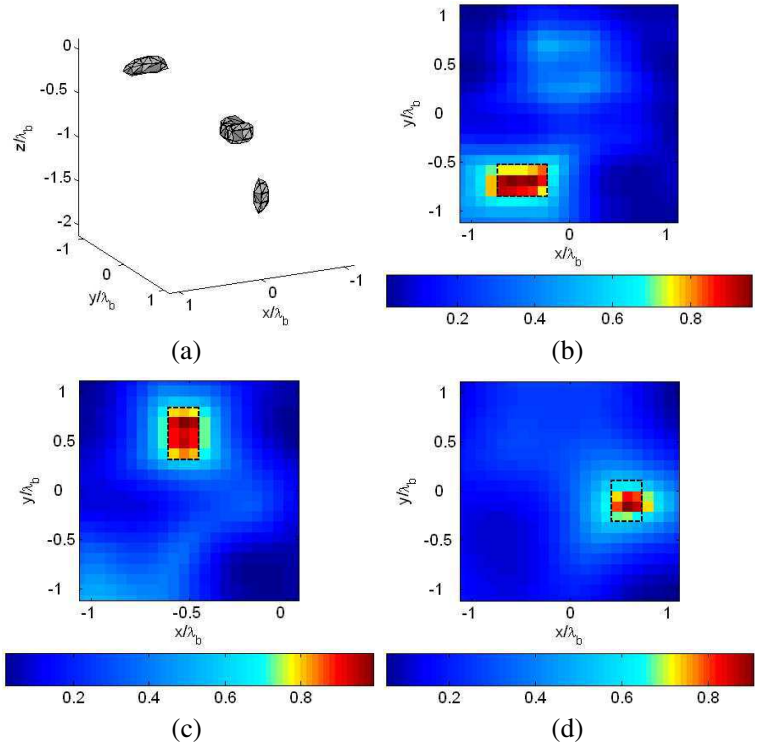

Figure 7. LSM indicator $[X/X_{\max}]_{dB}^{-1}$ for $N = 25$: (a) 3-D view; (b) slice at $z = -0.3\lambda_b$; (c) slice at $z = -0.7\lambda_b$; (d) slice at $z = -1.6\lambda_b$.

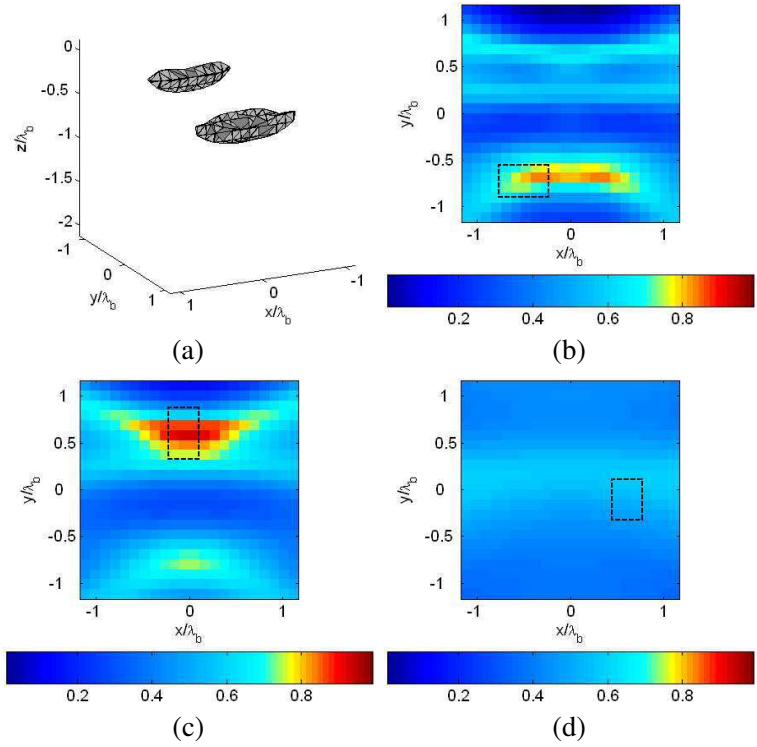

Figure 8. LSM indicator $[X/X_{\max}]_{dB}^{-1}$ for a linear array ($N = 5$): (a) 3-D view; (b) slice at $z = -0.3\lambda_b$; (c) slice at $z = -0.7\lambda_b$; (d) slice at $z = -1.6\lambda_b$.

linear array into 5 positions, with a $\lambda_b/2$ spacing, so to cover the whole 2-D measurement surface, the expected performance index is the one given in Fig. 9. As can it be observed, the map of $\tilde{\mathcal{E}}(5, 5, \underline{r})$ suggests that an improved result can be achieved in the shallower part of Ω, as compared to the single linear array case. This is confirmed by the plot of the support indicator X given in Figs. 10(a)–(d), which shows that results comparable to those achieved using the 2-D array can be obtained as far as the shallowest target is concerned. On the other hand, the reconstruction accuracy get worsen with depth, as the deeper target is still missed and the shape of the second target is only slightly improved compared to the single array case.

Finally, it is worth to remark that all the presented results require a processing time of a few seconds on a standard PC. Moreover, a good robustness against the noise affecting the data has been observed. As

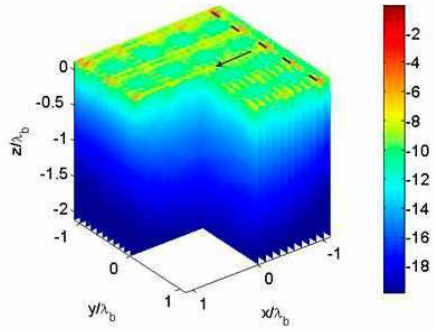

Figure 9. 3-D LSM expected performance index $\tilde{\mathcal{E}}(5, 5, \underline{r}_s)$.

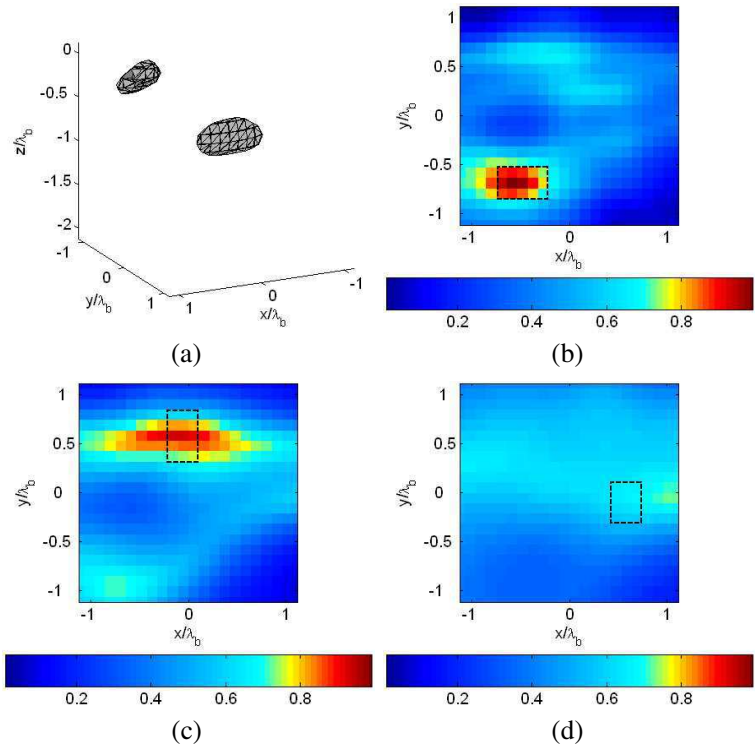

Figure 10. LSM indicator $[X/X_{\max}]_{dB}^{-1}$ for a moving a linear array ($N = 5$): (a) 3-D view; (b) slice at $z = -0.3\lambda_b$; (c) slice at $z = -0.7\lambda_b$; (d) slice at $z = -1.6\lambda_b$.

a matter of fact, results comparable to those shown in Figs. 7, 8, 10 have been obtained by assuming SNR values lower than 25 dB.

6. DISCUSSION AND CONCLUSIONS

The ongoing development of GPR systems based on antennas array has motivated us to consider the feasibility of the LSM for GPR surveys carried out in this configuration. In particular, we have exploited the spectral properties of integral operators describing the scattering phenomenon to derive tools, which allow to relate the performance of the LSM to the array aperture. Then, by means of 2-D and 3-D numerical examples, we have shown the effectiveness of these tools and assessed the capability of the LSM of operating (within the foreseen limits) also when very simple, though properly designed, array configurations are exploited. This is an interesting result, as LSM may represent a simple way to proceed towards actual 3-D surveys with feasible, almost negligible, computational cost.

As far as the observed limitation in the imaging of deeper targets is concerned, a possible way to counteract it is to juxtapose LSM reconstructions obtained at (few) different frequencies, so to combine the features of low frequency data in terms penetration with those of high frequency data in terms of achievable spatial resolution [20].

Finally, it is worth to note that the reasonings exploited to introduce the performance index and the footprints have a general validity, which makes them useful also in other cases.

ACKNOWLEDGMENT

The research leading to these results has received funding from the European Community's Seventh Framework Programme (FP7/2007-2013) under Grant Agreement 225663 Joint Call FP7-ICT-SEC-2007-1.

REFERENCES

1. Daniels, D. J., *Ground Penetrating Radar*, 2nd edition, The Institution of Electrical Engineers, London, UK, 2004.
2. Feng, X., F.-N. Kong, Z. Zeng, G. Fang, M. Sato, and Y. Hamada, "GPR using an array antenna for landmine detection," *Near Surface Geophysics*, Vol. 2, 3–9, 2004.

3. Aubry, P. J., L. P. Ligthart, A. G. Yarovoy, and T. G. Savelyev, "Array-based GPR for shallow subsurface imaging," *Proc. 4th Int. Workshop on Advanced GPR*, 12–15, 2007.
4. Payne, L. A., N. Linford, and P. Linford, "Stepped frequency ground-penetrating radar survey with a multi-element array antenna: Results from field application on archaeological sites," *Archaeol. Prospect.*, Vol. 17, 87–98, 2010.
5. Soldovieri, F., A. Brancaccio, G. Leone, and R. Pierri, "Shape reconstruction of perfectly conducting objects by multiview experimental data," *IEEE Trans. Geosci. Remote Sens.*, Vol. 43, No. 1, 65–71, 2005.
6. Catapano, I., L. Crocco, M. D'Urso, and T. Isernia, "A novel effective model for solving 3-D nonlinear inverse scattering problems in lossy scenarios," *IEEE Geosci. Remote Sens. Lett.*, Vol. 3, No. 3, 302–306, 2006.
7. Catapano, I., L. Crocco, R. Persico, M. Pieraccini, and F. Soldovieri, "Linear and nonlinear microwave tomography approaches for subsurface prospecting: Validation on real data," *IEEE Antennas Wireless Propagat. Lett.*, Vol. 5, No. 1, 49–53, 2006.
8. Fischer, C., A. Herschlein, M. Younis, and W. Wiesbeck, "Detection of antipersonnel mines by using the factorization method on multistatic ground-penetrating radar measurements," *IEEE Trans. Geosci. Remote Sens.*, Vol. 45, No. 1, 85–92, 2007.
9. Crocco, L., M. D'Urso, and T. Isernia, "The contrast source-extended born model for 2d subsurface scattering problems," *Progress In Electromagnetics Research B*, Vol. 17, 343–359, 2009.
10. Crocco, L., F. Soldovieri, T. Millington, and N. J. Cassidy, "Bistatic tomographic GPR imaging for incipient pipeline leakage evaluation," *Progress In Electromagnetics Research*, Vol. 101, 307–321, 2010.
11. Lo Monte, L., D. Erricolo, F. Soldovieri, and M. C. Wicks, "Radio frequency tomography for tunnel detection," *IEEE Trans. Geosci. Remote Sens.*, Vol. 48, No. 3, 1128–1137, 2010.
12. Huang Y., Y. Liu, Q. H. Liu, and J. Zhang, "Improved 3-D GPR detection by NUFFT combined with MPD method," *Progress In Electromagnetics Research*, Vol. 103, 185–199, 2010.
13. Soldovieri, F., O. Lopera, and S. Lambot, "Combination of advanced inversion techniques for an accurate target localization via GPR for demining applications," *IEEE Trans. Geosci. Remote Sens.*, Vol. 49, No. 1, 451–461, 2011.

14. Bermani, E., A. Boni, S. Caorsi, M. Donelli, and A. Massa, "A multi-source strategy based on a learning-by-examples technique for buried object detection," *Progress In Electromagnetics Research*, Vol. 48, 185–200, 2004.
15. Monk, P., D. Colton, and K. Giebermann, "A regularized sampling method for solving three dimensional inverse scattering problems," *SIAM J. Sci. Comput.*, Vol. 21, 2316–2330, 2000.
16. Cakoni, F. and D. Colton, *Qualitative Methods in Inverse Scattering Theory*, Springer-Verlag, Berlin, Germany, 2006.
17. Catapano, I., L. Crocco, and T. Isernia, "On simple methods for shape reconstruction of unknown scatterers," *IEEE Trans. Antennas Propagat.*, Vol. 55, 1431–1436, 2007.
18. Bertero, M. and P. Boccacci, *Introduction to Inverse Problems in Imaging*, Institute of Physics, Bristol, UK, 1998.
19. D'Urso, M., T. Isernia, I. Catapano, and L. Crocco, "3D microwave imaging via preliminary support reconstruction: Testing on the fresnel 2008 database," *Inverse Probl.*, Vol. 25, 024002, 2009.
20. Catapano, I., L. Crocco, and T. Isernia, "Improved sampling methods for shape reconstruction of 3-D buried targets," *IEEE Trans. Geosci. Remote Sens.*, Vol. 46, No. 10, 3265–3273, 2008.
21. Chew, W. C., *Waves Anf Fields in Inhomogeneous Media*, The Institute of Electrical and Electronics Engineers, Inc., Piscataway, NJ, 1995.
22. Catapano, I. and L. Crocco, "An imaging method for concealed targets," *IEEE Trans. Geosci. Remote Sens.*, Vol. 47, No. 5, 1301–1309, 2009.
23. Leone, G. and F. Soldovieri, "Analysis of the distorted Born approximation for subsurface reconstruction: Truncation and uncertainties effects," *IEEE Trans. Geosci. Remote Sens.*, Vol. 41, No. 1, 66–74, 2003.